

# Structure Elucidation of Complex Endotaxially Intergrown Lanthanum Barium Oxonitridosilicate Oxides by Combination of Microfocused Synchrotron Radiation and Transmission Electron Microscopy

Lisa Gamperl,<sup>[a]</sup> Lukas Neudert,<sup>[a, b]</sup> Peter Schultz,<sup>[b]</sup> Dajana Durach,<sup>[a]</sup> Wolfgang Schnick,<sup>\*[a]</sup> and Oliver Oeckler<sup>\*[b]</sup>

**Abstract:** Single-crystalline domains in intergrown microcrystalline material of the new compounds  $\text{Ba}_{22.5+x}\text{La}_{55-x}[\text{Si}_{129}\text{N}_{240-x}\text{O}_x]\text{O}_3\text{:Ce}^{3+}$  and  $\text{Ba}_{25.5+x}\text{La}_{77-x}[\text{Si}_{170}\text{N}_{312-x}\text{O}_{9+x}]\text{O}_4\text{:Ce}^{3+}$  were identified by transmission electron microscopy (TEM). Precise diffraction data from these domains were collected with microfocused synchrotron radiation so that crystal structure elucidation of the complex disordered networks became possible. They are composed of two different interconnected slabs of which one is similar in both compounds, which explains their notorious intergrowth. The

distribution of Ba and La is indicated by the analysis of bond-valence sums and by comparison with isostructural  $\text{Sr}_{28.5+x}\text{La}_{75-x}[\text{Si}_{170}\text{N}_{312-x}\text{O}_{9+x}]\text{O}_4$ .  $\text{Ce}^{3+}$  doping leads to yellow luminescence. This is a showcase that highlights the discovery and accurate characterization of new compounds relevant for luminescence applications from heterogeneous microcrystalline samples by exploiting the capability of the combination of TEM and diffraction using the latest focusing techniques for synchrotron radiation.


## Introduction


(Oxo-)nitridosilicates are an important class of compounds since they offer intriguing material properties. The compounds  $M_2\text{Si}_5\text{N}_8\text{:Eu}^{2+}$  ( $M = \text{Ca, Sr, Ba}$ ), for instance, constitute a prominent example as they made it into everyday use. These compounds are used in common amber-emitting phosphor-converted light emitting diodes (pcLEDs) adapted to specific requirements in the automotive field or general lighting.<sup>[1]</sup> Potential applications of (oxo-)nitridosilicates are diverse and cover a wide range from pcLEDs, for which  $\text{Eu}^{2+}$ - or  $\text{Ce}^{3+}$ -doped luminescent materials such as above mentioned  $M_2\text{Si}_5\text{N}_8\text{:Eu}^{2+}$  ( $M = \text{Ca, Sr, Ba}$ ) and  $M\text{Si}_2\text{O}_2\text{N}_2\text{:Eu}^{2+}$  ( $M = \text{Ca, Sr, Ba}$ ) are used, to lithium ion batteries, for example with ionic conductors like  $\text{Li}_4\text{Ln}_5[\text{Si}_{11}\text{N}_9\text{O}_5]\text{O}_2\text{F}_2$  ( $\text{Ln} = \text{Ce, Nd}$ ).<sup>[2–9]</sup> Even when new (oxo-)nitridosilicates exhibit no remarkable properties,

there is still great interest in elucidation of their crystal structures as the systematic crystal chemistry of (oxo-)nitridosilicates is still fragmentary. However, it is sometimes impossible to obtain sufficiently sized single crystals or phase pure powder samples from various syntheses, which often require extreme conditions, to elucidate the structure of new compounds with conventional single-crystal or powder X-ray diffraction.<sup>[10]</sup> Challenges concerning the structure determination of microcrystalline and often inhomogeneous samples have recently been approached by the combination of transmission electron microscopy (TEM) – especially selected area electron diffraction (SAED), scanning transmission electron microscopy (STEM) and energy dispersive X-ray spectroscopy (EDX) – with synchrotron methods that exploit the brilliance of microfocused X-ray beams.<sup>[11,12]</sup> Since the advent of compound refractive lenses,<sup>[13–16]</sup> synchrotron beams can be focused down to less than 1  $\mu\text{m}$ , which enables the collection of single-crystal X-ray data from crystallites with the same size that have been pre-characterized by TEM. This methodical combination enables the precise structural characterization of unique phases accessible only in form of crystallites with an interaction volume less than 1  $\mu\text{m}^3$ . So far, this approach has not been applied to get access to single-crystal data from samples that feature oriented intergrowth of different phases with overlapping diffraction patterns, which often impedes accurate crystal structure determination. Even if structure solution and refinement may be possible, the partial overlap of the individual reciprocal lattices is difficult to deal with; it reduces accuracy and may be ambiguous. Furthermore, synchrotron measurements provide high-resolution data, which are essential for an accurate structure solution and the combination of high-energy radiation and tiny crystals minimize absorption effects and associated artifacts. Exact knowledge of crystals structures is the

[a] L. Gamperl, L. Neudert, D. Durach, Prof. Dr. W. Schnick  
Department of Chemistry  
University of Munich (LMU)  
Butenandtstr. 5–13, 81377 Munich (Germany)  
E-mail: wolfgang.schnick@uni-muenchen.de

[b] L. Neudert, P. Schultz, Prof. Dr. O. Oeckler  
Institute for Mineralogy, Crystallography and Material Science  
Leipzig University  
Scharnhorststr. 20, 04275 Leipzig (Germany)  
E-mail: oliver.oeckler@gmx.de

 Supporting information for this article is available on the WWW under <https://doi.org/10.1002/chem.202101665>

 © 2021 The Authors. Chemistry - A European Journal published by Wiley-VCH GmbH. This is an open access article under the terms of the Creative Commons Attribution Non-Commercial NoDerivs License, which permits use and distribution in any medium, provided the original work is properly cited, the use is non-commercial and no modifications or adaptations are made.

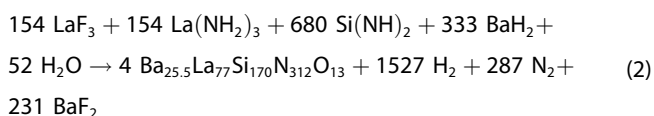
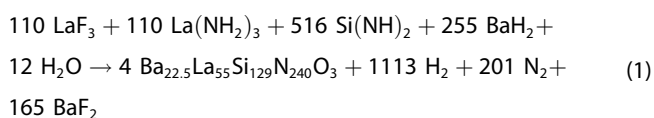
essential feature of the single-particle-diagnosis approach<sup>[17,18]</sup> as the basis for the derivation of structure-property relations and the overall understanding of (oxo)nitridosilicates. This aims at tuning properties so that they optimally suit the required applications of for example luminescent materials. The influence of the structure on luminescence properties has exemplarily been shown by investigations on the  $Sr_{1-x}Ba_xSi_2O_2N_2:Eu^{2+}$  phases.<sup>[19]</sup>

The combination of synchrotron and TEM is certainly expected to become more and more important in order to make accurate predictions and thus to control application-relevant properties. In this contribution, we report on the structure elucidation of two luminescent oxonitridosilicate oxides, namely  $Ba_{22.5+x}La_{55-x}[Si_{129}N_{240-x}O_x]O_3:Ce^{3+}$  and  $Ba_{25.5+x}La_{77-x}[Si_{170}N_{312-x}O_{9+x}]O_4:Ce^{3+}$  with intergrown complex structures. Single-crystalline domains were selected by TEM so that synchrotron diffraction data could be collected from the individual phases. The structure elucidation is supported by crystal-chemical considerations and comparison with  $Sr_{28.5+x}La_{75-x}[Si_{170}N_{312-x}O_{9+x}]O_4$  for the assignment of the cation distribution in isostructural  $Ba_{25.5+x}La_{77-x}[Si_{170}N_{312-x}O_{9+x}]O_4$ .

## Results and Discussion

### Synthesis and chemical analysis

The synthesis described in the Experimental Section led to  $Ba_{22.5+x}La_{55-x}[Si_{129}N_{240-x}O_x]O_3:Ce^{3+}$  ( $x \approx 0.24$ ) and  $Ba_{25.5+x}La_{77-x}[Si_{170}N_{312-x}O_{9+x}]O_4:Ce^{3+}$  ( $x \approx 0.24$ ) as luminescent crystallites, both present in the pale orange powder sample. Their formation may be explained according to the following idealized reaction equations (1) and (2) (all samples contain 2 mole% of  $Ce^{3+}$ , which is not always mentioned for the sake of conciseness):



TEM-EDX measurements (Tables S1, S2, Figure S1; “S” denotes Tables and Figures in the Supporting Information) of the crystals used for SCXRD led to an average atomic ratio Ba:La of about 1:2.1 for  $Ba_{22.5+x}La_{55-x}[Si_{129}N_{240-x}O_x]O_3$  and of about 1:2.6 for  $Ba_{25.5+x}La_{77-x}[Si_{170}N_{312-x}O_{9+x}]O_4$ . Within the typical limits of accuracy, this agrees with the values corresponding to the sum formulas derived from SCXRD data (Ba:La  $\approx$  1:2.4 and 1:3.3, respectively). The absolute values, however, somehow deviate from the expected ones. This can be explained by shadowing owing to the unfavorable orientation of the crystal with respect to the EDX detector; the values for Si, N and O are more strongly affected and thus determined too low compared to the values for

the heavier atoms Ba and La. Even though Ce as a dopant could not be detected by EDX, its occurrence is proven by the luminescence observed. Due to the small amount of Ce and the lack of scattering contrast between La and Ce, the latter was subsequently neglected in structure refinements. An IR spectrum of the sample shows no O–H or N–H vibrations and thus corroborates the absence of hydrogen in the reaction products (Figure S2a) as assumed due to the reaction conditions. Since both mixed and underoccupied cation sites are present, and since LaN vs. BaO can formally be exchanged for each other without violating charge neutrality, one may assume solid solutions  $Ba_{22.5+x}La_{55-x}[Si_{129}N_{240-x}O_x]O_3$  ( $x \approx 0.24$ ) and  $Ba_{25.5+x}La_{77-x}[Si_{170}N_{312-x}O_{9+x}]O_4$  ( $x \approx 0.24$ ). A Rietveld refinement based on the powder X-ray diffraction data using non refined atom parameters from single crystal data (see below) was performed for the determination of the bulk phase composition. The sample contains approximately 32 wt%  $Ba_{22.5+x}La_{55-x}[Si_{129}N_{240-x}O_x]O_3$  and approximately 68 wt%  $Ba_{25.5+x}La_{77-x}[Si_{170}N_{312-x}O_{9+x}]O_4$  (Figure 1, Table S3). The refinement therefore confirms the presence of the crystal structures elucidated by single-crystal analysis. Although according to the idealized reaction equations, a large amount of  $BaF_2$  should be formed, this was not found in the PXRD pattern. As described in literature,<sup>[20]</sup> it is possible that binary halides formed during the reaction deposit on the inside wall of the water-cooled silica glass reactor through transport reactions at high reaction temperatures.

$Sr_{28.5+x}La_{75-x}[Si_{170}N_{312-x}O_{9+x}]O_4:Ce^{3+}$  ( $x \approx -3.71$ ) was synthesized analogous to the Ba compound according to the following idealized reaction equation (3):

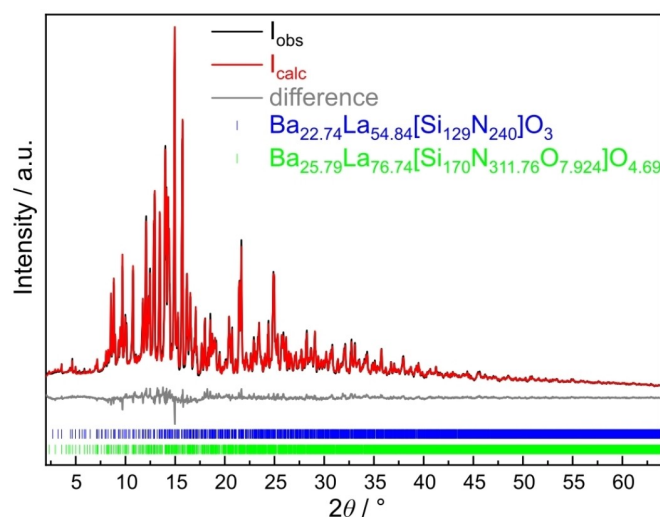
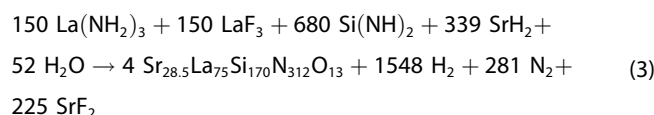


**Figure 1.** Rietveld refinement based on PXRD data (Mo- $K\alpha_1$  radiation,  $\lambda = 0.70930 \text{ \AA}$ ) collected from a sample containing  $Ba_{22.5+x}La_{55-x}[Si_{129}N_{240-x}O_x]O_3$  with  $x \approx 0.24$  (32 wt%) and  $Ba_{25.5+x}La_{77-x}[Si_{170}N_{312-x}O_{9+x}]O_4$  with  $x \approx 0.24$  (68 wt%) based on the structure models obtained by SCXRD data.

TEM-EDX measurements (Table S4) of the single crystal used for synchrotron SCXRD resulted in a Sr:La ratio of about 1:1 compared to the theoretical value from the single crystal X-ray data of Sr:La  $\approx$  1:3.3. This deviation is again due to pronounced shadowing, which reduces the amount of emitted Sr X-rays reaching the detector. For other crystals less suitable for synchrotron data collection due to their too small volume, inferior crystal quality or unfavorable positions on the TEM grid, higher Sr contents were detected. IR spectroscopy again confirms the absence of hydrogen in the reaction products (Figure S2b). Rietveld refinement using powder X-ray diffraction data (Figure S3, Table S5) shows that  $\text{Sr}_{28.5+x}\text{La}_{75-x}[\text{Si}_{170}\text{N}_{312-x}\text{O}_{9+x}]\text{O}_4$  was obtained as a side phase (approx. 28 wt%) alongside  $\text{La}_{13.68}\text{Sr}_{12.32}[\text{Si}_{60}\text{N}_{96}]\text{F}_{6.32}\text{O}_{5.68}^{[21]}$  (approx. 72 wt%) and a small amount of an additional unknown phase. Although the latter's reflections could neither be assigned to an already known phase nor indexed,  $R_{\text{Bragg}}$  values of 0.0425 for  $\text{Sr}_{28.5+x}\text{La}_{75-x}[\text{Si}_{170}\text{N}_{312-x}\text{O}_{9+x}]\text{O}_4$  and 0.0244 for  $\text{La}_{13.68}\text{Sr}_{12.32}[\text{Si}_{60}\text{N}_{96}]\text{F}_{6.32}\text{O}_{5.68}$  confirm the presence of these compounds.

### Diffraction patterns

Since only crystals with maximum sizes up to 10  $\mu\text{m}$  (Figure 2a–c) along with low scattering volumes were obtained for the three compounds and structure solution based on the PXRD data was impeded by samples that were not phase pure, a microfocused synchrotron beam was used for collecting single crystal X-ray diffraction data.

The combined analysis of reciprocal lattice sections reconstructed from synchrotron X-ray data of several crystallites and SAED patterns as part of preceding TEM characterization (Figures 2, S4) showed systematically absent classes of reflections that were incompatible with systematic absences of any space group (Figure 2i and 2m). The observed diffraction patterns could also not be explained assuming non-merohedral twinning. However, further electron diffraction experiments revealed a superposition of SAED patterns of two different types. Patterns along different viewing directions with respect to the two different unit cells can be completely interpreted assuming oriented intergrowth with a  $30^\circ$  tilt (Figure 2f) of two compounds with hexagonal metrics: type 1 with  $a \approx 17.5 \text{ \AA}$  and  $c \approx 22.7 \text{ \AA}$  (blue lattice in Figure 2, S4) and type 2 with  $a \approx 20.2 \text{ \AA}$  and  $c \approx 22.7 \text{ \AA}$  (red lattice in Figures 2, S4). The  $c$  lattice parameters are similar and with respect to  $a$ , the following relations are valid:  $a_2 = \sqrt{3}a_1/2$ ,  $3V_2 = 4V_1$  and  $a_1 = \cos(30^\circ) \cdot a_2 = \cos(30^\circ) \cdot 20.2 \text{ \AA} \approx 17.5 \text{ \AA}$ . The  $2mm$  and  $6$  symmetry of the SAED patterns along zone axis  $\langle 100 \rangle$  and  $[001]$ , respectively, correspond to hexagonal  $P$  lattices and suggest Laue class  $6/m$ . The observed reflection positions match those of simulated ones assuming this intergrowth. TEM-EDX measurements revealed the two intergrown phases as barium lanthanum oxonitridosilicates with different Ba:La ratios (type 1  $\approx$  1:2 and type 2  $\approx$  1:3, Figure S4b). This insight forced the search for non-intergrown crystallites of each compound by SAED and EDX. In extensive TEM investigations, separate single

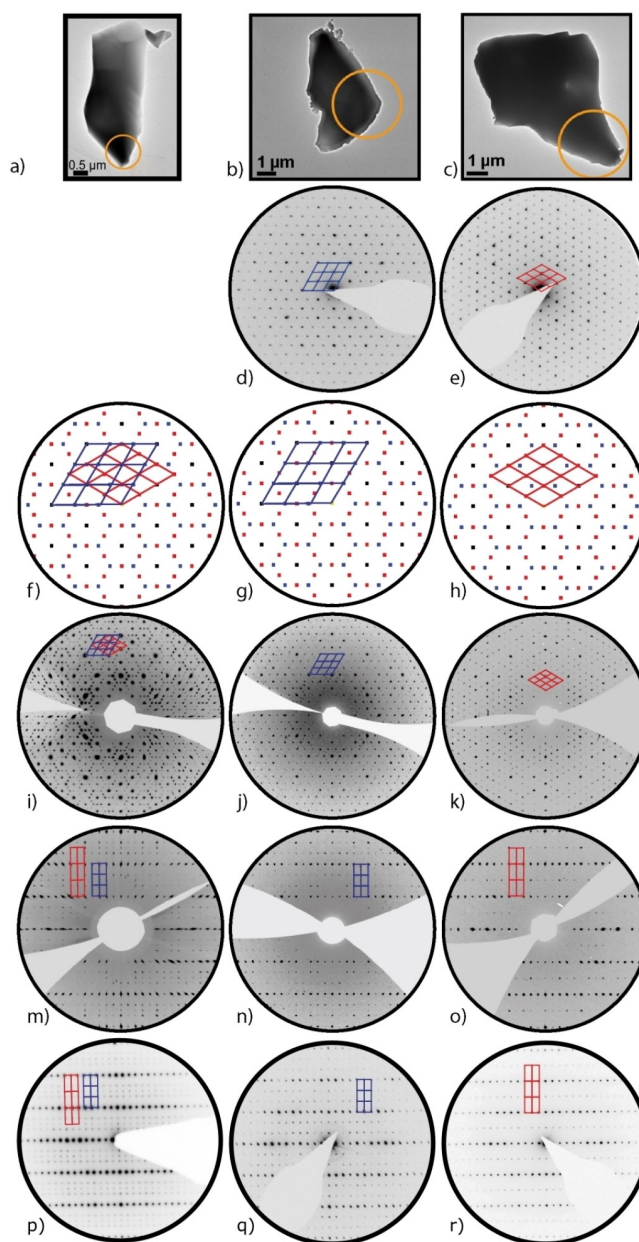


**Figure 2.** TEM bright-field images of a) an intergrown crystal as well as b)  $\text{Ba}_{22.5+x}\text{La}_{55-x}[\text{Si}_{129}\text{N}_{240-x}\text{O}_x]\text{O}_3$  ( $a \approx 17.5 \text{ \AA}$ ) and c)  $\text{Ba}_{25.5+x}\text{La}_{77-x}[\text{Si}_{170}\text{N}_{312-x}\text{O}_{9+x}]\text{O}_4$  ( $a \approx 22.7 \text{ \AA}$ ) single crystals. All sections corresponding to the crystallites shown in (a–c) are depicted in the same column. d) and e) SAED patterns along  $[001]$  for both crystallites. f–h) Sketched reciprocal lattices with lattice nodes of  $\text{Ba}_{22.5+x}\text{La}_{55-x}[\text{Si}_{129}\text{N}_{240-x}\text{O}_x]\text{O}_3$  in blue and  $\text{Ba}_{25.5+x}\text{La}_{77-x}[\text{Si}_{170}\text{N}_{312-x}\text{O}_{9+x}]\text{O}_4$  in red along  $[001]$ . i–k) Reciprocal lattice sections  $hk0$ . m–o) Reciprocal lattice sections  $Ok_l$  for  $\text{Ba}_{22.5+x}\text{La}_{55-x}[\text{Si}_{129}\text{N}_{240-x}\text{O}_x]\text{O}_3$ ,  $h\bar{2}hl$  for  $\text{Ba}_{25.5+x}\text{La}_{77-x}[\text{Si}_{170}\text{N}_{312-x}\text{O}_{9+x}]\text{O}_4$  and their overlapping pattern. p–r) SAED patterns along  $[100]$  for all variants. Note that reciprocal lattice sections of the  $\text{Ba}_{22.5+x}\text{La}_{55-x}[\text{Si}_{129}\text{N}_{240-x}\text{O}_x]\text{O}_3$  crystal exhibit very weak reflections of the second variant (Figure 2j, honeycomb-like patterns near the beam stop).

crystallites of both variants were identified. The structure models of the two related oxonitridosilicate frameworks were determined from synchrotron X-ray diffraction data of the sub-micron-sized crystallites characterized by TEM, which were re-located at the beamline using X-ray fluorescence scans. For

$\text{Sr}_{28.5+x}\text{La}_{75-x}[\text{Si}_{170}\text{N}_{312-x}\text{O}_{9+x}]\text{O}_4$ , suitable crystallites were identified by TEM in a similar fashion and diffraction data were also collected with microfocused synchrotron radiation. The data revealed a new phase with hexagonal metrics similar to that of type 2 but Sr instead of Ba leading to shorter lattice parameters ( $a = 19.6$ ,  $c = 21.9$  Å, Figure S4d).

### Crystal-structure determination

In all structure analyses, the distribution of elements with low scattering contrast such as the combinations N/O and Ba/La was analyzed using bond-valence sum (BVS) calculations.<sup>[22–24]</sup> The structure solution of  $\text{Ba}_{22.5+x}\text{La}_{55-x}[\text{Si}_{129}\text{N}_{240-x}\text{O}_x]\text{O}_3$  in space group  $P\bar{6}$  with direct methods yielded mainly heavy atom (La, Ba) and Si atom positions, light atoms were localized in subsequent difference Fourier syntheses. An only moderately higher  $R_{\text{sym}} = 0.122$  for the higher Laue symmetry  $6/mmm$  compared to  $R_{\text{sym}} = 0.072$  for  $6/m$  indicated merohedral twinning (twin law  $010|100|00\bar{1}$ ). Taking this into account decreased  $R1$  from 0.219 to 0.047 with a resulting twin ratio of 64.4(1):35.6. The refinement was further checked for additional inversion twinning. However, volume fractions for the domains with inverted structure were not significant (less than one standard deviation); therefore, inversion twinning was not taken into account. A three-dimensional tetrahedra network was obtained. However, some hypothetical Si atom positions located unrealistically close to each other turned out to be split heavy-atom positions as the coordinating light atoms are located at typical interatomic distances in La/Ba–N/O bonds. The total occupancy of split-atom pairs was set to 100%, which was consistent with the scattering density observed. The occupancy of the non-split La/Ba17 position refined to a value of 0.55(3), which agreed with that of the nearby split position La/Ba5B while being too close to the alternative site La/Ba5A. The positional shift of La/Ba5A relative to La/Ba5B can easily be explained as a cation vacancy on the La/Ba17 position is balanced by rearrangement of nearby cations (Figure S5). The occupancy factors of La/Ba17 and La/Ba5B were thus constrained to be equal without a significant increase in  $R$  values. In order to validate the presence of split positions in space group  $P\bar{6}$ , twin refinements in lower symmetries were performed, always taking merohedral twinning into account as suggested by group-subgroup relations. Direct subgroups  $P3$  (additional mirror twinning) and  $Pm$  (additional threefold rotation twinning) yielded rather unstable refinements unless displacement parameters of atoms, which are equivalent in  $P\bar{6}$ , were constrained to the same values. Space group  $P1$  was also tentatively tested. These calculations did not yield ordered models as they still show the same split positions in difference Fourier syntheses as the model in  $P\bar{6}$ . One example for  $Pm$ , which theoretically enables ordering, is shown in the difference Fourier maps of Figure S6. The simultaneous presence of Ba/La and O/N impedes the determination of the atom distribution with X-ray methods due to lacking scattering contrast. Furthermore, the charge-neutral exchange BaO vs. LaN renders the use of charge neutrality constraints impractical. Bond-

valence sum (BVS) calculations require some presumptions as derived Ba:La ratios depend on the O/N distribution and vice versa. According to various examples in literature and very low O contents suggested by EDX, initially a model with only  $\text{SiN}_4$  tetrahedra was considered.<sup>[10,25,26]</sup> Discrete non-tetrahedral anions were assigned as O in both cases according to Pauling's rule and as their distances of 2.26(2) Å to the nearest cations are in the range of La–O bonds but too short for La–N bonds.<sup>[27–29]</sup> Ba:La ratios for each position were then derived by BVS (Table S6) and transferred with minor corrections to achieve charge neutrality to the single-crystal structure refinements as fixed values. During the refinements, the obtained model was repeatedly checked for plausibility based on EDX data,  $R$ -values, residual electron density as well as cation-anion distances and adjusted if necessary. Some cation positions turned out not to be fully occupied. Charge neutrality was achieved by adapting the values from BVS calculations with minor corrections.

For the structure determination of  $\text{Ba}_{25.5+x}\text{La}_{77-x}[\text{Si}_{170}\text{N}_{312-x}\text{O}_{9+x}]\text{O}_4$ , a similar approach was applied. In this case, the simultaneous presence of the analogous Sr compound was a great advantage because, in contrast to Ba and La, Sr and La have different scattering factors and can thus be distinguished by X-ray diffraction. Due to the notorious intergrowth of crystals of the two Ba compounds, it is likely that their structures are closely related, at least with respect to their lattices, but possibly also concerning their symmetry and atom arrangement. It turned out that they exhibit the same space group  $P\bar{6}$ . The structures of  $\text{Ba}_{25.5+x}\text{La}_{77-x}[\text{Si}_{170}\text{N}_{312-x}\text{O}_{9+x}]\text{O}_4$  and  $\text{Sr}_{28.5+x}\text{La}_{75-x}[\text{Si}_{170}\text{N}_{312-x}\text{O}_{9+x}]\text{O}_4$  were solved by direct methods and as they turned out to be similar, they were refined simultaneously. The SCXRD data of the Sr compound were used to identify all sites that are completely occupied by La atoms, which in addition was supported by BVS calculations (Tables S7, S8). These sites were then identified in the Ba containing compound and also assumed to be completely occupied by La atoms. Sites not fully occupied by La atoms were assumed to be mixed occupied with Sr and La. To determine whether these sites completely occupied by a mixture of both atoms, it was checked whether the corresponding sites in the Ba containing compound are fully occupied when refined as La atoms, since La and Ba exhibit almost the same scattering factor. This information, including possible vacancies, was again transferred to the Sr compound, for which then the mixed occupation was refined and the obtained occupation was applied to the Ba compound and not further refined. Discrete non-tetrahedral anions were assigned as O in both compounds, while threefold bridging anions were set as N according to Pauling's rule.<sup>[40]</sup> Terminal anions were assumed with a mixed O/N occupancy restoring charge neutrality, whereas twofold bridging anions were solely defined as N. During the refinement process, the results were continuously checked for plausibility based on BVS calculations, EDX data,  $R$ -values, residual electron density as well as cation-anion distances and adjusted if necessary to achieve charge neutrality. The structure refinement of type 2 is also supported by STEM-HAADF at atomic resolution viewed along special directions (Figure S7a–c). Z-contrast images along

zone axis [100] showed similar heavy atom positions of the type 2 La/Ba and La/Sr oxonitridosilicates and suggest isotopic crystal structures (Figure S7c, d).

Important crystallographic data is given in Table 1. Atomic coordinates, isotropic displacement parameters, site occupancy factors (Table S9, S11, S13) as well as anisotropic displacement parameters (Table S10, S12, S14) for all three compounds are summarized in the Supporting Information.

### Structure description

Both  $\text{Ba}_{22.5+x}\text{La}_{55-x}[\text{Si}_{129}\text{N}_{240-x}\text{O}_x]\text{O}_3$ ,  $\text{Ba}_{25.5+x}\text{La}_{77-x}[\text{Si}_{170}\text{N}_{312-x}\text{O}_{9+x}]\text{O}_4$  and  $\text{Sr}_{28.5+x}\text{La}_{75-x}[\text{Si}_{170}\text{N}_{312-x}\text{O}_{9+x}]\text{O}_4$  crystallize in space group  $P\bar{6}$  and show very similar crystal structures built up from vertex- and edge-sharing  $\text{Si}(\text{N/O})_4$  tetrahedra. The three-dimensional networks can formally be divided into two interconnected layers (Figure 3). The layer depicted in blue and red color in Figure 3 is present in all three compounds and consists of triple tetrahedral sharing one vertex (orange in Figure 4), which are aligned in one plane but tilted with respect to each

**Table 1.** Crystallographic data of the single-crystal structure determinations of  $\text{Ba}_{22.5+x}\text{La}_{55-x}[\text{Si}_{129}\text{N}_{240-x}\text{O}_x]\text{O}_3$ ,  $\text{Ba}_{25.5+x}\text{La}_{77-x}[\text{Si}_{170}\text{N}_{312-x}\text{O}_{9+x}]\text{O}_4$  and  $\text{Sr}_{28.5+x}\text{La}_{75-x}[\text{Si}_{170}\text{N}_{312-x}\text{O}_{9+x}]\text{O}_4$ .

formula	$\text{Ba}_{22.74}\text{La}_{54.84}[\text{Si}_{129}\text{N}_{240}]\text{O}_3$	$\text{Ba}_{25.79}\text{La}_{76.74}[\text{Si}_{170}\text{N}_{311.76}\text{O}_{9.24}]\text{O}_4$	$\text{Sr}_{24.79}\text{La}_{78.75}[\text{Si}_{170}\text{N}_{315.71}\text{O}_{5.24}]\text{O}_4$
formula mass/g mol <sup>-1</sup>	17774.9	23556.8	22458.3
crystal system		hexagonal	
space group		$P\bar{6}$ (no. 174)	
lattice parameters/Å	$a = 17.480(1)$ $c = 22.687(2)$	$a = 20.137(1)$ $c = 22.644(2)$	$a = 20.048(1)$ $c = 22.524(1)$
cell volume/Å <sup>3</sup>	6003.3(9)	7951.9(1)	7840.0(9)
Z		1	
X-ray density/g cm <sup>-3</sup>	4.916	4.919	4.758
abs. coefficient $\mu/\text{mm}^{-1}$	7.334	3.199	5.715
absorption correction		semiempirical	
temperature/K		294(2)	
radiation		synchrotron ( $\lambda = 0.41325 \text{ \AA}$ )	synchrotron ( $\lambda = 0.2947 \text{ \AA}$ )
$F(000)$	7909	10486.7	10095.1
$\theta$ range/°	$1.56 \leq \theta \leq 16.44$	$2.08 \leq \theta \leq 17.17$	$1.49 \leq \theta \leq 12.15$
independent reflections	10726	16414	14855
refined parameters/restraints	520/0	677/299	461/299
GoF	1.199	1.181	1.517
$R_{\text{int}}$	0.0823	0.0604	0.0866
$R_{\sigma}$	0.0700	0.0553	0.0678
$R1$ (all data/for $I > 2\sigma(I)$ )	0.0469/0.0449	0.0415/0.0397	0.0860/0.0775
$wR2$ (all data/for $I > 2\sigma(I)$ )	0.1102/0.1083	0.0956/0.0947	0.1785/0.1737

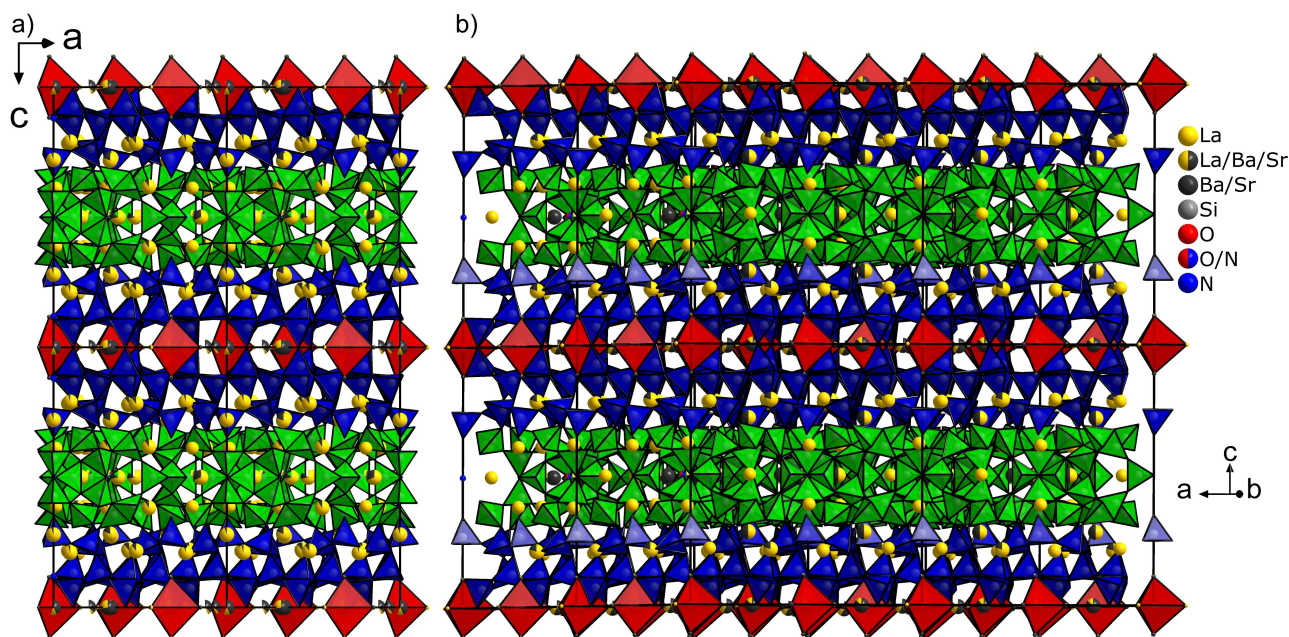


**Figure 3.** Crystal structures of a)  $\text{Ba}_{22.5+x}\text{La}_{55-x}[\text{Si}_{129}\text{N}_{240-x}\text{O}_x]\text{O}_3$  and b)  $\text{Ba}_{25.5+x}\text{La}_{77-x}[\text{Si}_{170}\text{N}_{312-x}\text{O}_{9+x}]\text{O}_4$  viewed along [010]. The structure of  $\text{Ba}_{25.5+x}\text{La}_{77-x}[\text{Si}_{170}\text{N}_{312-x}\text{O}_{9+x}]\text{O}_4$  is homeotypic to  $\text{Sr}_{28.5+x}\text{La}_{75-x}[\text{Si}_{170}\text{N}_{312-x}\text{O}_{9+x}]\text{O}_4$ .  $\text{Si}(\text{N/O})_4$  tetrahedra in blue and green,  $\text{O}(\text{La/Ba})_3$  polyhedra in red; unit cell outlined in black.

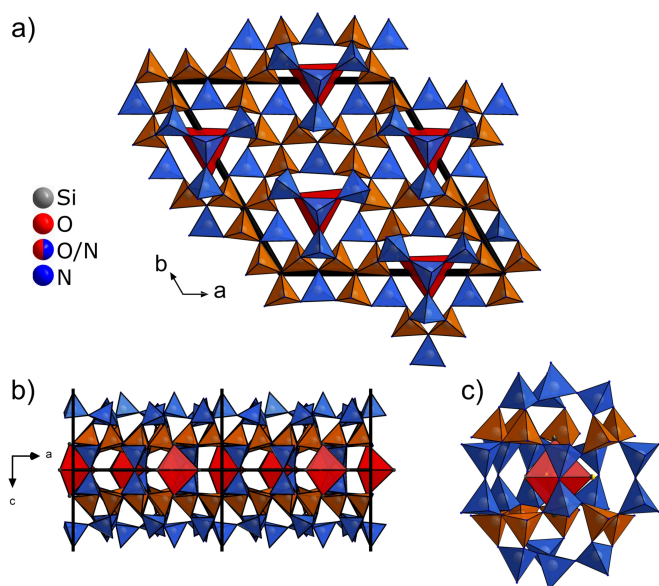


**Figure 4.** a) Structure of the layer that occurs both in  $\text{Ba}_{22.5+x}\text{La}_{55-x}[\text{Si}_{129}\text{N}_{240-x}\text{O}_x]\text{O}_3$  and  $\text{Ba}_{25.5+x}\text{La}_{77-x}[\text{Si}_{170}\text{N}_{312-x}\text{O}_{9+x}]\text{O}_4$  (similar to  $\text{Sr}_{28.5+x}\text{La}_{75-x}[\text{Si}_{170}\text{N}_{312-x}\text{O}_{9+x}]\text{O}_4$ ) viewed along [001]; b) same layer viewed along [010]; c) cage of  $\text{Si}(\text{N}/\text{O})_4$  tetrahedra around an  $\text{O}(\text{La}/\text{Ba})_5$  trigonal bipyramid (red);  $\text{Si}(\text{N}/\text{O})_4$  tetrahedra in blue and orange; unit cell outlined in black.

other (Figure 4b) and interconnected according to the scheme shown in Figure 4a. Two adjacent triple tetrahedra units are connected via three vertices of single tetrahedra with inverted orientation in the same plane as well as by tetrahedra (blue) connecting two tetrahedron vertices. Three of those tetrahedra are linked by another tetrahedron above the “missing” triple tetrahedra unit. This arrangement is mirrored (Figure 4b), and therefore forms *achter* ring cages.<sup>[30]</sup> The cavity of those cages is filled by an unbound oxygen atom, which is coordinated by five La/Ba/Sr atoms in a distorted trigonal bipyramid (Figure 4c, red). This similar layer might be the reason for the intergrowth of  $\text{Ba}_{22.5+x}\text{La}_{55-x}[\text{Si}_{129}\text{N}_{240-x}\text{O}_x]\text{O}_3$  and  $\text{Ba}_{25.5+x}\text{La}_{77-x}[\text{Si}_{170}\text{N}_{312-x}\text{O}_{9+x}]\text{O}_4$  single crystallites. The compounds differ with respect to the structure of the second layer (green layers in Figure 3), which is the same for  $\text{Ba}_{25.5+x}\text{La}_{77-x}[\text{Si}_{170}\text{N}_{312-x}\text{O}_{9+x}]\text{O}_4$  and  $\text{Sr}_{28.5+x}\text{La}_{75-x}[\text{Si}_{170}\text{N}_{312-x}\text{O}_{9+x}]\text{O}_4$  with the exception of the cation occupancies. In  $\text{Ba}_{22.5+x}\text{La}_{55-x}[\text{Si}_{129}\text{N}_{240-x}\text{O}_x]\text{O}_3$ , this layer consists of three different units (Figure 5).

Three tetrahedra form a *dreier* ring (blue, Figure 5b), which interconnects three units built up from six tetrahedra each (darker green, Figure 5c) via shared corners. In this entity, two pairs of tetrahedra share a common edge and are interconnected by the remaining two tetrahedra via shared vertices, forming a branched *vierer* ring. Two of these units are linked via one shared vertex and mapped onto one another by a mirror plane. These units are again interconnected by pairs of tetrahedra (red, Figure 5d) around the mirror plane.

A closely related, but different layer can be found in  $\text{Ba}_{25.5+x}\text{La}_{77-x}[\text{Si}_{170}\text{N}_{312-x}\text{O}_{9+x}]\text{O}_4$  (Figure 6). One third of the blue *dreier* rings with only twofold bridging N is replaced by a triple tetrahedra unit (yellow, Figure 6b) with one threefold bridging,

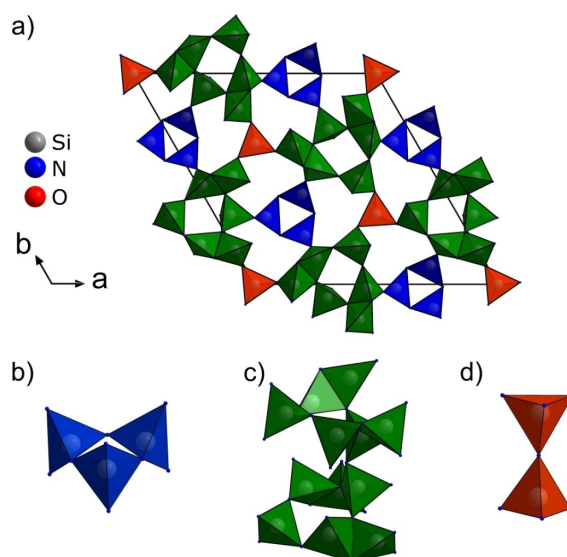


**Figure 5.** a) Structure of the layer occurring in  $\text{Ba}_{22.5+x}\text{La}_{55-x}[\text{Si}_{129}\text{N}_{240-x}\text{O}_x]\text{O}_3$  viewed along [001]; b) *dreier* ring unit; c) pair of *vierer* rings; d) pair of tetrahedra.  $\text{Si}(\text{N}/\text{O})_4$  tetrahedra in blue, green and red; unit cell outlined in black.

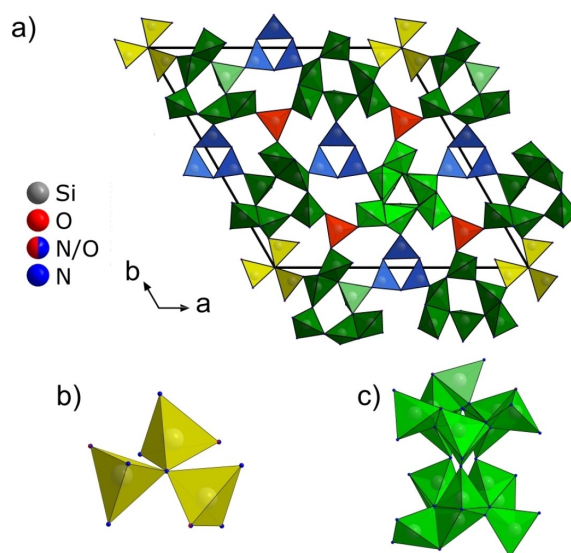


**Figure 6.** a) Structure of the layer occurring in  $\text{Ba}_{25.5+x}\text{La}_{77-x}[\text{Si}_{170}\text{N}_{312-x}\text{O}_{9+x}]\text{O}_4$  and  $\text{Sr}_{28.5+x}\text{La}_{75-x}[\text{Si}_{170}\text{N}_{312-x}\text{O}_{9+x}]\text{O}_4$  viewed along [001]; b) triple tetrahedron unit; c) disordered unit.  $\text{Si}(\text{N}/\text{O})_4$  tetrahedra in blue, green and red; unit cell outlined in black.

three terminal N/O and six twofold bridging N atoms in the same plane. Furthermore, one third of the branched *vierer* ring units (darker green), which are oriented differently, is replaced by a disordered unit (lighter green, Figure 6c) that is formed by superposition of three units, each of which is only occupied by one third, respectively. These units emerge from each other by a  $120^\circ$  rotation of one of the units along [001] (Figure 7).

The basic unit is built from five tetrahedra, of which two share an edge whereas the remaining ones share vertices. These

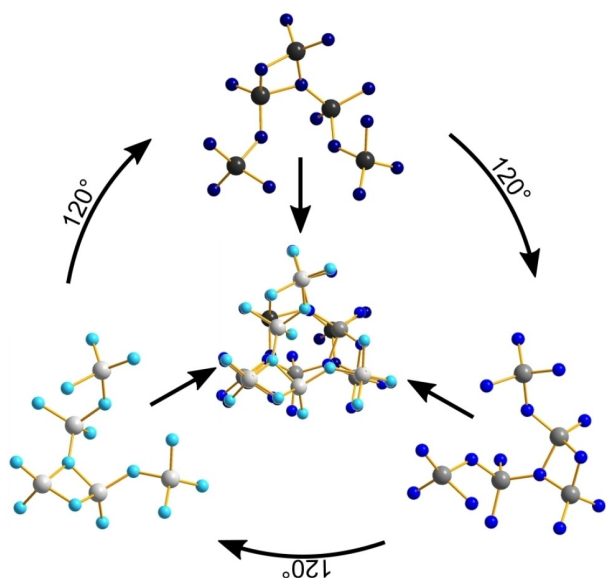


**Figure 7.** Schematic interpretation of the disordered unit resulting from the superposition of three entities linked by the threefold axis along [001]. Si atoms in shades of gray, N atoms in shades of blue. As a simplification, the sites with mixed O/N occupations were solely occupied by N.

units were identified by difference Fourier syntheses taking into account the underlying symmetry operations, respective. The superposition is due to the fact that the size of possibly ordered, lower symmetry domains is smaller than the X-ray's length of coherence.

For all three compounds discussed, interatomic distances within the Si–N/O tetrahedra, O–La/Ba and O–La/Sr distances as well as the cation coordination polyhedra with the corresponding distances are listed in Tables S15–18 and agree well with those reported for other (oxo-)nitridosilicates.<sup>[31–44]</sup>

## Luminescence

Photoluminescence properties were measured on a Ce<sup>3+</sup> doped (2 mol-%) thick-bed powder sample containing both Ba<sub>22.5+x</sub>La<sub>55-x</sub>[Si<sub>129</sub>N<sub>240-x</sub>O<sub>x</sub>]O<sub>3</sub> and Ba<sub>25.5+x</sub>La<sub>77-x</sub>[Si<sub>170</sub>N<sub>312-x</sub>O<sub>9+x</sub>]O<sub>4</sub>. The sample shows yellow luminescence upon irradiation with UV to blue light ( $\lambda_{\text{exc}} = 440$  nm) with an emission maximum at  $\lambda_{\text{em}} \approx 588$  nm and a full width at half-maximum (fwhm) of about 166 nm/4541 cm<sup>-1</sup> (Figure 8).

The maximum intensity of the excitation spectrum is located approximately at 455 nm, so the material can be excited very well by blue light as emitted by a (Ga,In)N-LED. The luminescence probably originates from both compounds present in the sample. Comparison of the charges and ionic radii indicates that Ce<sup>3+</sup> (CN=6–9: 1.01–1.20 Å) preferably replaces La<sup>3+</sup> (CN=6–9: 1.03–1.22 Å) rather than the larger Ba<sup>2+</sup>.<sup>[45]</sup> The broadband emission of the 5d–4f transition of Ce<sup>3+</sup> corresponds to a superposition of light emitted from various low-symmetrical and chemically different cation sites with surroundings of mixed N/O occupancy present in both

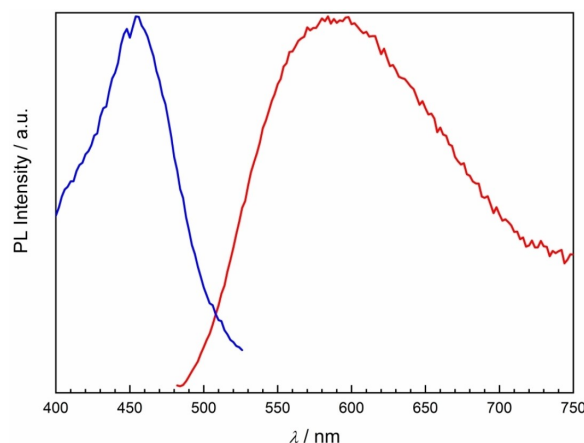


**Figure 8.** Normalized excitation (blue) and emission spectra (red,  $\lambda_{\text{exc}} = 440$  nm) of a sample containing Ba<sub>22.5+x</sub>La<sub>55-x</sub>[Si<sub>129</sub>N<sub>240-x</sub>O<sub>x</sub>]O<sub>3</sub>:Ce<sup>3+</sup> and Ba<sub>25.5+x</sub>La<sub>77-x</sub>[Si<sub>170</sub>N<sub>312-x</sub>O<sub>9+x</sub>]O<sub>4</sub>:Ce<sup>3+</sup>.

compounds.<sup>[46,47]</sup> Comparison of the emission characteristics with other LED phosphor materials such as La<sub>3</sub>BaSi<sub>5</sub>N<sub>9</sub>O<sub>2</sub>:Ce<sup>3+</sup> ( $\lambda_{\text{em}} \approx 578$  nm, fwhm  $\approx 167$  nm/4700 cm<sup>-1</sup>, 12 cation sites),<sup>[48]</sup> CaAlSiN<sub>3</sub>:Ce<sup>3+</sup> ( $\lambda_{\text{em}} \approx 570$ –603 nm, fwhm  $\approx 150$  nm/3900 cm<sup>-1</sup>, 1 cation site),<sup>[49]</sup> (La,Ca)<sub>3</sub>Si<sub>6</sub>N<sub>11</sub>:Ce<sup>3+</sup> ( $\lambda_{\text{em}} \approx 577$ –581 nm, fwhm  $\approx 130$ –143 nm/3760–3960 cm<sup>-1</sup>, 2 cation sites)<sup>[50]</sup> and Y<sub>3</sub>Al<sub>5</sub>O<sub>12</sub>:Ce<sup>3+</sup> ( $\lambda_{\text{em}} \approx 550$ –570 nm, fwhm  $\approx 3700$  cm<sup>-1</sup>, 1 cation site)<sup>[51]</sup> all with fewer cation sites than Ba<sub>22.5+x</sub>La<sub>55-x</sub>[Si<sub>129</sub>N<sub>240-x</sub>O<sub>x</sub>]O<sub>3</sub> (21 cation sites) and Ba<sub>25.5+x</sub>La<sub>77-x</sub>[Si<sub>170</sub>N<sub>312-x</sub>O<sub>9+x</sub>]O<sub>4</sub> (27 cation sites) shows that the observed emission of the latter compounds is not particularly broader despite the larger number of cation sites. Further investigations of the luminescence properties of single-phase materials would be required to clarify the influence of their slightly different structures on the individual luminescence properties.

## Conclusion

Ba<sub>22.5+x</sub>La<sub>55-x</sub>[Si<sub>129</sub>N<sub>240-x</sub>O<sub>x</sub>]O<sub>3</sub>, Ba<sub>25.5+x</sub>La<sub>77-x</sub>[Si<sub>170</sub>N<sub>312-x</sub>O<sub>9+x</sub>]O<sub>4</sub> and Sr<sub>28.5+x</sub>La<sub>75-x</sub>[Si<sub>170</sub>N<sub>312-x</sub>O<sub>9+x</sub>]O<sub>4</sub> were obtained as microcrystallites through high-temperature solid-state reactions. Extensive TEM investigations enabled the discovery of endotaxially intergrown Ba<sub>22.5+x</sub>La<sub>55-x</sub>[Si<sub>129</sub>N<sub>240-x</sub>O<sub>x</sub>]O<sub>3</sub> and Ba<sub>25.5+x</sub>La<sub>77-x</sub>[Si<sub>170</sub>N<sub>312-x</sub>O<sub>9+x</sub>]O<sub>4</sub> domains. Single-crystalline fragments of each phase were identified by electron diffraction. Due to the small crystallite size, microfocused synchrotron radiation was essential for the collection of single-crystal data and thus the elucidation of the crystal structures, which was supported by BVS calculations and STEM imaging. As Sr and La can be distinguished by X-ray methods, the determination of the cation distribution in Ba<sub>25.5+x</sub>La<sub>77-x</sub>[Si<sub>170</sub>N<sub>312-x</sub>O<sub>9+x</sub>]O<sub>4</sub> was substantially supported by the discovery of the analogous compound Sr<sub>28.5+x</sub>La<sub>75-x</sub>[Si<sub>170</sub>N<sub>312-x</sub>O<sub>9+x</sub>]O<sub>4</sub>. The two new structure types feature complex, rather similar silicate networks. The presence of similar layers explains the notorious intergrowth of Ba<sub>22.5+x</sub>La<sub>55-x</sub>[Si<sub>129</sub>N<sub>240-x</sub>O<sub>x</sub>]O<sub>3</sub> and Ba<sub>25.5+x</sub>La<sub>77-x</sub>[Si<sub>170</sub>N<sub>312-x</sub>O<sub>9+x</sub>]O<sub>4</sub>

O<sub>4</sub>. The difference between these is due to a second type of layer that is characteristic for each phase. A sample containing both compounds shows broad yellow luminescence upon doping with Ce<sup>3+</sup>. Compared to phosphors with similar emission characteristics but fewer cation sites, the reported compounds do not show significantly broader emission. These compounds represent yet another example for a complex structure with interesting luminescence properties. Disorder does not have a negative effect on these properties, quite similar to the situation in Sr<sub>1-x</sub>Ba<sub>x</sub>Si<sub>2</sub>O<sub>2</sub>N<sub>2</sub>:Eu<sup>2+</sup> phases.<sup>[6,17,52-54]</sup> The elucidation of such complex crystal structures in microcrystalline samples with intergrown domains would not have been possible a few years ago because they rely on advances both concerning the development of TEM methods and focusing of synchrotron beam. The search for new compounds will probably lead to more and more complex structures and therefore, in future research, microfocussed synchrotron radiation assisted by TEM studies are expected to become an established tool that can provide high resolution data for accurate structure information even with smallest crystallites. Such data enable more precise statements about structure-property relations and may indicate how to optimally tune materials for required applications.

## Experimental Section

**Synthesis:** Due to air and moisture sensitivity of some starting materials, all preparation steps were carried out under argon atmosphere either in an argon-filled glovebox (Unilab, MBraun, Garching; O<sub>2</sub> < 1 ppm; H<sub>2</sub>O < 1 ppm) or in argon filled glassware (Schlenk technique). For the synthesis of Ba<sub>22.5+x</sub>La<sub>55-x</sub>[Si<sub>129</sub>N<sub>240-x</sub>O<sub>x</sub>]O<sub>3</sub> and Ba<sub>25.5+x</sub>La<sub>77-x</sub>[Si<sub>170</sub>N<sub>312-x</sub>O<sub>9+x</sub>]O<sub>4</sub>, a thoroughly ground mixture of 20.1 mg La(NH<sub>2</sub>)<sub>3</sub> (0.108 mmol),<sup>[55]</sup> 20.3 mg LaF<sub>3</sub> (0.104 mmol, Sigma-Aldrich, 99.99%), 66.3 mg BaH<sub>2</sub> (0.476 mmol, Chemco, 99.7%), 35.6 mg silicon diimide (0.613 mmol),<sup>[56]</sup> and 0.8 mg CeF<sub>3</sub> as dopant (0.004 mmol, 2 mol-%, Sigma-Aldrich, 99.99%) was filled into a tungsten crucible, which was then transferred into the water-cooled silica glass reactor of a radio-frequency furnace (AXIO 10/450, max. output 10 kW, Hüttinger Elektronik, Freiburg) attached to a Schlenk line. H<sub>2</sub>O may be present due to partial hydrolysis of the starting materials, especially amides and imides. The crucible was heated under N<sub>2</sub>-atmosphere to 1600 °C within one hour.<sup>[57]</sup> After maintaining the temperature for 10 h, the crucible was slowly cooled to 900 °C within 44 h. The product was finally quenched by switching off the furnace. The orange Ce-doped microcrystalline powder shows yellow luminescence under irradiation with UV to blue light. Sr<sub>28.5+x</sub>La<sub>75-x</sub>[Si<sub>170</sub>N<sub>312-x</sub>O<sub>9+x</sub>]O<sub>4</sub> was synthesized starting from 20.1 mg La(NH<sub>2</sub>)<sub>3</sub> (0.108 mmol),<sup>[55]</sup> 20.3 mg LaF<sub>3</sub> (0.104 mmol, Sigma-Aldrich, 99.99%), 42.7 mg SrH<sub>2</sub> (0.476 mmol), 35.6 mg silicon diimide (0.613 mmol),<sup>[56]</sup> H<sub>2</sub>O due to partial hydrolysis and 0.8 mg CeF<sub>3</sub> (0.004 mmol, 2 mol-%, Sigma-Aldrich, 99.99%) applying the same temperature program. This also led to an orange microcrystalline powder. All products are insensitive against oxygen and H<sub>2</sub>O.

**Transmission electron microscopy:** For investigations using transmission electron microscopy, the polycrystalline samples were crushed, dispersed in absolute ethanol and drop-cast on carbon-film-coated copper grids, which were then fixed on double-tilt low-background holders. For STEM, SAED and EDX measurements, a Titan 80–300 (FEI, USA) with a field emission gun (FEG) operated at 300 kV and equipped with a TOPS 30 EDX spectrometer (EDAX,

Germany), an UltraScan 1000 camera (Gatan, USA, resolution: 2k × 2k) as well as a Titan Themis 60–300 (FEI, USA) with a cold FEG operated at 300 kV acceleration voltage equipped with a X-FEG emitter, monochromator, C<sub>s</sub> corrector and windowless four-quadrant Super-X EDX detector were used. In the latter setup, images were acquired using a Ceta CMOS camera (FEI, USA) with a resolution of 4k × 4k. High resolution transmission electron microscopy (HRTEM) and SAED data were evaluated using the programs Digital Micrograph (e.g. for Fourier filtering of the HRTEM images) and JEMS for SAED simulations.<sup>[58,59]</sup> EDX data were processed with ES Vision.<sup>[60]</sup>

**Single-crystal X-ray diffraction:** Single-crystal X-ray diffraction (SCXRD) data of Ba<sub>22.5+x</sub>La<sub>55-x</sub>[Si<sub>129</sub>N<sub>240-x</sub>O<sub>x</sub>]O<sub>3</sub>, Ba<sub>25.5+x</sub>La<sub>77-x</sub>[Si<sub>170</sub>N<sub>312-x</sub>O<sub>9+x</sub>]O<sub>4</sub> and Sr<sub>28.5+x</sub>La<sub>75-x</sub>[Si<sub>170</sub>N<sub>312-x</sub>O<sub>9+x</sub>]O<sub>4</sub> were collected at beamline ID11 of the ESRF in Grenoble, France (Ge(111) double-crystal monochromator, Frelon4 K CCD detector).<sup>[61]</sup> Suitable single crystallites had previously been identified by SAED and TEM-EDX. The crystallites on TEM grids were centered in the synchrotron beam by a large-magnification telescope and using X-ray fluorescence linescans for La as described in literature.<sup>[11]</sup> The beam was microfocussed with a Be/Al refractive lens system.<sup>[13-16]</sup> Diffraction data were evaluated with the CrysAlis program suite.<sup>[62]</sup> Scaling and semi-empirical absorption correction were performed with SADABS and structure solution and refinement with SHELX-2014.<sup>[63,64]</sup> In order to account for the systematic error owing to the diffraction-angle dependence of the beam path through the CCD phosphor, a beam-incidence correction was applied.<sup>[65]</sup> Deposition Numbers 1958352 (for Ba<sub>22.5+x</sub>La<sub>55-x</sub>[Si<sub>129</sub>N<sub>240-x</sub>O<sub>x</sub>]O<sub>3</sub>), 1958355 (for Ba<sub>25.5+x</sub>La<sub>77-x</sub>[Si<sub>170</sub>N<sub>312-x</sub>O<sub>9+x</sub>]O<sub>4</sub>) and 1864686 (for Sr<sub>28.5+x</sub>La<sub>75-x</sub>[Si<sub>170</sub>N<sub>312-x</sub>O<sub>9+x</sub>]O<sub>4</sub>) contain the supplementary crystallographic data for this paper. These data are provided free of charge by the joint Cambridge Crystallographic Data Centre and Fachinformationszentrum Karlsruhe Access Structures service.

**Powder X-ray diffraction:** Powder X-ray diffraction (PXRD) data were obtained from finely ground samples sealed into glass capillaries (0.2 mm diameter, wall thickness 0.01 mm; Hilgenberg GmbH, Malsfeld, Germany) using a Stoe StadiP diffractometer (Mo-Kα<sub>1</sub> radiation, λ = 0.70930 Å, Stoe & Cie, Darmstadt, Germany) equipped with an Ge(111) monochromator and a Mythen1 K detector (Dectris, Baden-Dättwil, Switzerland) in parafocusing modified Debye-Scherrer geometry. Rietveld refinements based on the collected data were performed using the TOPAS Academic V6 package applying the fundamental parameters approach (direct convolution of source emission profiles, axial instrument contributions, crystallite size and microstrain effects).<sup>[66-68]</sup> Corrections of the absorption effects were performed using the calculated absorption coefficient. Preferred orientation was modelled using spherical harmonics of fourth order. The structure models obtained from single-crystal synchrotron X-ray diffraction data were used as a starting point for all refinements, in which only lattice parameters were refined, while atomic coordinates, site occupations and isotropic displacement parameters were kept fixed.

**IR spectroscopy:** Fourier transform infrared (FTIR) spectra were recorded with a BXII spectrometer (PerkinElmer, Rodgau, Germany) mounting ATR (attenuated total reflection) technology.

**Luminescence:** Photoluminescence properties of microcrystalline Ba<sub>22.5+x</sub>La<sub>55-x</sub>[Si<sub>129</sub>N<sub>240-x</sub>O<sub>x</sub>]O<sub>3</sub> and Ba<sub>25.5+x</sub>La<sub>77-x</sub>[Si<sub>170</sub>N<sub>312-x</sub>O<sub>9+x</sub>]O<sub>4</sub> powder samples were measured in PTFE sample holders using an in-house built system based on a 5.3" integrating sphere and a spectrofluorimeter equipped with a 150 W Xe lamp, two 500 mm Czerny-Turner monochromators, 1800 1/mm lattices and 250/500 nm lamps with a spectral range from 230 to 820 nm.



## Acknowledgements

The European Synchrotron Radiation Facility (ESRF, Grenoble, France) is acknowledged for granting beamtime (projects CH-4318 and CH-4612) and travel support. The authors thank Petra Huppertz, Detlef Wiechert, and Volker Weiler (all at Lumileds Phosphor Center, Aachen, Germany) for luminescence measurements. Dr. Vadim Dyadkin (ESRF, Grenoble, France), Dr. Felix Fahrnbauer, Dr. Stefan Schwarz Müller, Dr. Markus Nentwig and Dr. Frank Heinke (all at Leipzig University) are acknowledged for help with the synchrotron measurements. Inspiring discussions with Dr. Christian Maak (Department of Chemistry, LMU) are gratefully appreciated. Open access funding enabled and organized by Projekt DEAL.

## Conflict of Interest

The authors declare no conflict of interest.

**Keywords:** electron microscopy · high-temperature chemistry · luminescence · microcrystals · microfocused synchrotron radiation

- [1] a) R. Mueller-Mach, G. O. Mueller, M. R. Krames, O. B. Shchekin, P. J. Schmidt, H. Bechtel, C.-H. Chen, O. Steigelmann, *Phys. Status Solidi RRL* **2009**, *3*, 215–217; b) PB62 LUXEON Rebel Phosphor-Converted Amber Product Brief. Lumileds Holding B. V. **2009**; c) PB109 LUXEON F PC Amber Product Brief. Lumileds Holding B. V. **2018**.
- [2] M. Zeuner, S. Pagano, W. Schnick, *Angew. Chem. Int. Ed.* **2011**, *50*, 7754–7775; *Angew. Chem.* **2011**, *123*, 7898–7920.
- [3] H. A. Höpfe, H. Lutz, P. Morys, W. Schnick, A. Seilmeier, *J. Phys. Chem. Solids* **2000**, *61*, 2001–2006.
- [4] H. A. Höpfe, F. Stadler, O. Oeckler, W. Schnick, *Angew. Chem. Int. Ed.* **2004**, *43*, 5540–5542; *Angew. Chem.* **2004**, *116*, 5656–5658.
- [5] J. A. Kechele, O. Oeckler, F. Stadler, W. Schnick, *Solid State Sci.* **2009**, *11*, 537–543.
- [6] R. Müller-Mach, G. Müller, M. R. Krames, H. A. Höpfe, F. Stadler, W. Schnick, T. Jüstel, P. Schmidt, *Phys. Status Solidi A* **2005**, *202*, 1727–1732.
- [7] H. Höpfe, *Angew. Chem. Int. Ed.* **2009**, *48*, 3572–3582; *Angew. Chem.* **2009**, *121*, 3626–3636.
- [8] P. Pust, P. J. Schmidt, W. Schnick, *Nat. Mater.* **2015**, *14*, 454–458.
- [9] S. Lupart, G. Gregori, J. Maier, W. Schnick, *J. Am. Chem. Soc.* **2012**, *134*, 10132–10137.
- [10] D. Durach, P. Schultz, O. Oeckler, W. Schnick, *Inorg. Chem.* **2016**, *55*, 3624–3629.
- [11] F. Fahrnbauer, T. Rosenthal, T. Schmutzler, G. Wagner, G. B. M. Vaughan, J. P. Wright, O. Oeckler, *Angew. Chem. Int. Ed. Engl.* **2015**, *54*, 10020–10023; *Angew. Chem.* **2015**, *127*, 10158–10161.
- [12] S. D. Kloß, L. Neudert, M. Döblinger, M. Nentwig, O. Oeckler, W. Schnick, *J. Am. Chem. Soc.* **2017**, *139*, 12724–12735.
- [13] G. B. M. Vaughan, J. P. Wright, A. Bytchkov, C. Curfs, C. Grundlach, M. Orlova, L. Erra, H. Gleyzolle, T. Buslaps, A. Götz, G. Suchet, S. Petitdemange, M. Rossat, L. Margulies, W. Ludwig, A. Snigirev, I. Snigireva, H. O. Sorensen, E. M. Lauridsen, U. L. Olsen, J. Oddershede, H. F. Poulsen, *Challenges in Materials Science Possibilities in 3D and 4D Characterization Techniques: Proceedings of the 31st Risø International Symposium on Materials Science*; Technical University of Denmark, Lyngby, Denmark, **2010**, 457–476.
- [14] G. B. M. Vaughan, J. P. Wright, A. Bytchkov, M. Rossat, H. Gleyzolle, I. Snigireva, A. Snigirev, *J. Synchrotron Radiat.* **2011**, *18*, 125–133.
- [15] B. Lengeler, C. Schroer, J. Tümmler, B. Benner, M. Richwin, A. Snigirev, I. Snigireva, M. Drakopoulos, *J. Synchrotron Radiat.* **1999**, *6*, 1153–1167.
- [16] B. Lengeler, C. G. Schroer, B. Benner, A. Gerhardus, T. F. Günzler, M. Kuhlmann, J. Meyer, C. Zimprich, *J. Synchrotron Radiat.* **2002**, *9*, 119–124.
- [17] X.-J. Wang, L. Wang, T. Takeda, S. Funahashi, T. Suehiro, N. Hirotsaki, R.-J. Xie, *Chem. Mater.* **2015**, *27*, 7689–7697.
- [18] N. Hirotsaki, T. Takeda, S. Funahashi, R.-J. Xie, *Chem. Mater.* **2014**, *26*, 4280–4288.
- [19] M. Seibald, T. Rosenthal, O. Oeckler, W. Schnick, *Crit. Rev. Solid State Mater. Sci.* **2014**, *39*, 215–229.
- [20] C. Maak, D. Durach, C. Martiny, P. J. Schmidt, W. Schnick, *Chem. Mater.* **2018**, *30*, 3552–3558.
- [21] D. Durach, W. Schnick, *Z. Anorg. Allg. Chem.* **2016**, *642*, 101–106.
- [22] A. S. Wills, *Valist*, v. 4.0.7, University College London, UK, **2010**.
- [23] N. E. Brese, M. O’Keeffe, *Acta Crystallogr. Sect. B* **1991**, *47*, 192–197.
- [24] I. D. Brown, D. Altermatt, *Acta Crystallogr. Sect. B* **1985**, *41*, 244–247.
- [25] D. Durach, W. Schnick, *Eur. J. Inorg. Chem.* **2015**, *24*, 4095–4100.
- [26] L. Neudert, D. Durach, F. Fahrnbauer, G. B. M. Vaughan, W. Schnick, O. Oeckler, *Inorg. Chem.* **2017**, *56*, 13070–13077.
- [27] P. E. D. Morgan, *J. Mater. Sci.* **1986**, *21*, 4305–4309.
- [28] N. Garg, K. K. Pandey, C. Murlu, K. V. Shanavas, B. P. Mandal, A. K. Tyagi, S. M. Sharma, *Phys. Rev. B* **2008**, *77*, 214105, 1–8.
- [29] S. B. Schneider, D. Baumann, A. Salamat, W. Schnick, *J. Appl. Phys.* **2012**, *111*, 093503, 1–6.
- [30] The term *dreier* (*vierer*, *achter*) ring was established by F. Liebau and is derived from the German word “dreier” (“vierer”, “achter”). A *dreier* (*vierer*, *achter*) ring comprises three (four, eight) tetrahedra centers. F. Liebau, *Structural Chemistry of Silicates*, Springer, Berlin, **1985**.
- [31] H. Yamane, F. J. DiSalvo, *J. Alloys Compd.* **1996**, *240*, 33–36.
- [32] Z. A. Gal, P. R. Mallinson, H. J. Orchard, S. J. Clarke, *Inorg. Chem.* **2004**, *43*, 3998–4006.
- [33] D. Wilhelm, M. Seibald, D. Baumann, K. Wurst, H. Huppertz, *Eur. J. Inorg. Chem.* **2018**, *2018*, 731–738.
- [34] C. Maak, L. Eisenburger, J. P. Wright, M. Nentwig, P. J. Schmidt, O. Oeckler, W. Schnick, *Inorg. Chem.* **2018**, *57*, 13840–13846.
- [35] Z. Inoue, T. Sawada, K. Ohsumi, M. Mitomo, R. Sadanaga, *Acta Crystallogr. Sect. A* **1981**, *37*, C154.
- [36] M. Woike, W. Jeitschko, *Inorg. Chem.* **1995**, *34*, 5105–5108.
- [37] K. Liddell, D. P. Thompson, *J. Mater. Chem.* **2001**, *11*, 507–512.
- [38] H. Müller-Bunz, T. Schleid, *Z. Anorg. Allg. Chem.* **2000**, *626*, 2549–2556.
- [39] M. Abed, H. K. Müller-Buschbaum, *J. Alloys Compd.* **1992**, *190*, 61–64.
- [40] K.-I. Machida, G.-Y. Adachi, J. Shiokawa, M. Shimada, M. Koizumi, *Acta Crystallogr. Sect. B* **1982**, *38*, 386–389.
- [41] C. Schmolke, D. Bichler, D. Johrendt, W. Schnick, *Solid State Sci.* **2009**, *11*, 389–394.
- [42] C. Schmolke, S. Lupart, W. Schnick, *Solid State Sci.* **2009**, *11*, 305–309.
- [43] T. Schlieper, W. Milius, W. Schnick, *Z. Anorg. Allg. Chem.* **1995**, *621*, 1380–1384.
- [44] H. Huppertz, W. Schnick, *Z. Anorg. Allg. Chem.* **1997**, *623*, 212–217.
- [45] R. D. Shannon, *Acta Crystallogr. Sect. A* **1976**, *32*, 751–767.
- [46] A. Meijerink, G. Blasse, *J. Lumin.* **1989**, *43*, 283–289.
- [47] G. Blasse, B. C. Grabmaier, *Luminescent Materials*, Springer, Berlin, Heidelberg, NY, **1994**.
- [48] D. Durach, L. Neudert, P. J. Schmidt, O. Oeckler, W. Schnick, *Chem. Mater.* **2015**, *27*, 4832–4838.
- [49] Y. Q. Li, N. Hirotsaki, R.-J. Xie, T. Takeda, M. Mitomo, *Chem. Mater.* **2008**, *20*, 6704–6714.
- [50] T. Suehiro, N. Hirotsaki, R.-J. Xie, *ACS Appl. Mater. Interfaces* **2011**, *3*, 811–816.
- [51] T. Moriguchi, Y. Noguchi, K. Sakanao, Y. Shimizu, US 5998925 A, **1997**.
- [52] M. Seibald, T. Rosenthal, O. Oeckler, F. Fahrnbauer, A. Tücks, P. J. Schmidt, W. Schnick, *Chem. Eur. J.* **2012**, *18*, 13446–13452.
- [53] M. Seibald, O. Oeckler, V. R. Celinski, P. J. Schmidt, A. Tücks, W. Schnick, *Solid State Sci.* **2011**, *13*, 1769–1778.
- [54] M. Seibald, T. Rosenthal, O. Oeckler, C. Maak, A. Tücks, P. J. Schmidt, D. Wiechert, W. Schnick, *Chem. Mater.* **2013**, *25*, 1852–1857.
- [55] C. Hadenfeldt, B. Gieger, H. Jacobs, *Z. Anorg. Allg. Chem.* **1974**, *410*, 104–112.
- [56] H. Lange, G. Wötting, G. Winter, *Angew. Chem. Int. Ed.* **1991**, *30*, 1579–1597; *Angew. Chem.* **1991**, *103*, 1606–1625.
- [57] W. Schnick, H. Huppertz, R. Lauterbach, *J. Mater. Chem.* **1999**, *9*, 289–296.
- [58] *Digital Micrograph v3.6.1*, Gatan Software Team, Pleasanton, USA, **1999**.
- [59] a) P. A. Stadelmann, *Ultramicroscopy* **1987**, *21*, 131–145; b) P. A. Stadelmann, *JEMS v3.3425U2008*, CIME-EPFL, Switzerland, **1999–2008**.
- [60] *ES Vision v4.0.164*, Emispec Systems Inc., Tempe, USA, **1994–2002**.
- [61] J. C. Labiche, O. Mathon, S. Pascarelli, M. A. Newton, G. G. Ferre, C. Curfs, G. Vaughan, A. Homs, D. F. Carreiras, *Rev. Sci. Instrum.* **2007**, *78*, 091301, 1–11.

- [62] *CrysAlisPro 1.171.38.41*, Rigaku Oxford Diffraction, **2015**.
- [63] G. M. Sheldrick, *SADABS, v. 2: Multi-Scan Absorption Correction*; Bruker-AXS, Billerica, MA, **2012**.
- [64] G. M. Sheldrick, *Acta Crystallogr. Sect. C* **2015**, *71*, 3–8.
- [65] G. Wu, B. L. Rodrigues, P. Coppens, *J. Appl. Crystallogr.* **2002**, *35*, 356–359.
- [66] A. A. Coelho, TOPAS Version 6: A program for Rietveld refinement, Coelho Software **2016**.
- [67] J. Bergmann, R. Kleeberg, A. Haase, B. Breidenstein, *Mater. Sci. Forum* **2000**, *347–349*, 303–308.
- [68] R. W. Cheary, A. A. Coelho, J. P. Cline, *J. Res. Natl. Inst. Stand. Technol.* **2004**, *109*, 1–25.

---

Manuscript received: May 10, 2021  
Accepted manuscript online: July 9, 2021  
Version of record online: August 3, 2021

---